IEEE Access
Multidisciplinary | Rapid Review | Open Access Journal

Received May 12, 2022, accepted June 5, 2022, date of publication June 16, 2022, date of current version June 23, 2022.

Digital Object Identifier 10.1109/ACCESS.2022.3183746

Deep Learning Implementation of Model Predictive Control for Multioutput Resonant Converters

PABLO GUILLÉN[1], (Student Member, IEEE), FELIX FIEDLER[2], HÉCTOR SARNAGO[1], (Senior Member, IEEE), SERGIO LUCÍA[2], (Member, IEEE), AND ÓSCAR LUCÍA[1], (Senior Member, IEEE)

[1]Department of Electronic Engineering and Communications, I3A, University of Zaragoza, 50018 Zaragoza, Spain
[2]Laboratory of Process Automation Systems, Technische Universität Dortmund, 44227 Dortmund, Germany

Corresponding author: Pablo Guillén (pguillenm@unizar.es)

This work was supported in part by the Spanish MICINN and AEI co-funded by EU through FEDER Program under Project PID2019-103939RB-I00 and Project PDC2021-120898-I00, in part by DGAFSE, in part by MECD through FPU under Grant FPU17/01442 and Grant EST21/00298, and in part by the BSH Home Appliances Group.

ABSTRACT Flexible-surface induction cooktops rely on multi-coil structures which are powered by means of advanced resonant power converters that achieve high versatility while maintaining high efficiency and power density. The study of multi-output converters has led to cost-effective and reliable implementations even if they present complex control challenges to provide high performance. For this scenario, model predictive control arises as a modern control technique that is capable of handling multivariable problems while dealing with nonlinearities and constraints. However, these controllers are based on the computationally-demanding solution of an optimization problem, which is a challenge for high-frequency real-time implementations. In this context, deep learning presents a potent solution to approximate the optimal control policy while achieving a time-efficient evaluation, which permits an online implementation. This paper proposes and evaluates a multi-output-resonant-inverter model predictive controller and its implementation on an embedded system by means of a deep neural network. The proposal is experimentally validated by a resonant converter applied to domestic induction heating featuring a two-coil 3.6 kW architecture controlled by means of a FPGA.

INDEX TERMS Home appliances, induction heating, model predictive control, multi-output inverter, neural network, power control.

I. INTRODUCTION

Flexible surface induction heating appliances combine the main induction heating advantages, such as high efficiency, fast heating and safe and clean operation, with the pot detection capabilities in order to boost user experience [1]–[3].

The increased flexibility is achieved by multi-coil structures as the ones depicted in Figure 1. In order to power these structures, several alternatives of resonant power converters have been proposed in the literature. The alternatives include classical single-inverter single-coil implementations [4], [5], load multiplexation approaches [6], and a heterogeneous group of multi-output inverters [7]–[11].

All of these topologies provide versatile and reliable solutions that require complex modulation strategies in order to achieve proper and precise power management [12], [13]. In order to do so, an increasing number of control parameters is required and several constraints arise, leading to limited application of classical control techniques. In this context, model predictive control (MPC) appears as an effective tool to control multi-in multi-out complex systems [14], with a high applicability in the field of power electronics [15]–[18].

MPC uses a model of the system in order to predict its behavior and is therefore able to compute a sequence of control inputs by solving an optimization problem that optimizes a desired performance.

The online solution of the optimization problem presents limitations when applied to high frequency power electronics, leading to solutions that require strong simplifications [17].

The associate editor coordinating the review of this manuscript and approving it for publication was Atif Iqbal.

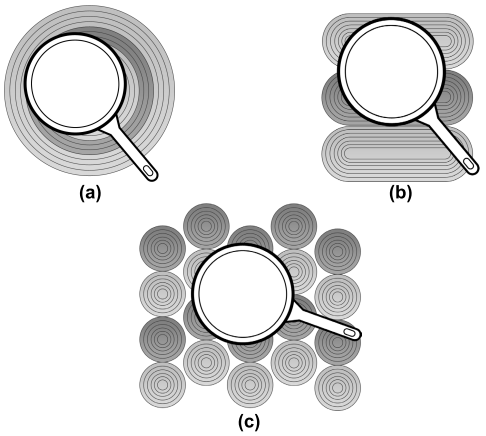

FIGURE 1. Flexible induction heating alternative layouts. Size flexibility (a), vertical flexibility (b), and complete flexibility (c).

However, at its core, the MPC problem can be seen as an implicit function, mapping the current state to an optimal control input. Therefore, with the widespread development of deep learning, approaches that solve rigorous nonlinear MPC and implement it by means of a deep neural network (DNN) have been proposed in the literature [19]–[21], being applicable to resonant converters [22], [23].

This work proposes the formulation of a general nonlinear MPC for a multi-output resonant inverter, whose control law is then implemented in a DNN. The MPC is designed to solve a multi-load power-tracking control while dealing with shared power devices, and therefore common control parameters. Additionally, the optimization problem includes non-linear constraints to ensure the converter high efficiency and safe operation, e.g. zero voltage switch commutation. The DNN is designed such that a low approximation error of the NMPC is achieved while being implementable in a FPGA and solved in in real time, within the same switching cycle, at 30 kHz. The proposed approach is implemented and verified experimentally on a 3.6 kW multi-output inverter.

The remainder of this paper is organized as follows. Section II presents the multi-output converter and Sections III and IV cover the MPC design and DNN learning, respectively. Section V shows the experimental results and Section VI concludes this article.

II. MULTI-OUTPUT RESONANT INVERTER

In order to achieve cost-effective implementations, reduced idle power devices, and decrease mean time between failures, multi-output inverters have been proposed to power flexible surface cooktops. These implementations are derived from different single output classical converters, such as the half-bridge [11], [24], full bridge [25] or single switch topologies [26], [27].

A recurrent approach consists on reducing the number of power devices by sharing some of them among the different loads [27]–[29]. As a consequence, classical modulation strategies are limited in the power control, requiring the inclusion of independent parameters that correspond with the independent power devices [12], [13], [30].

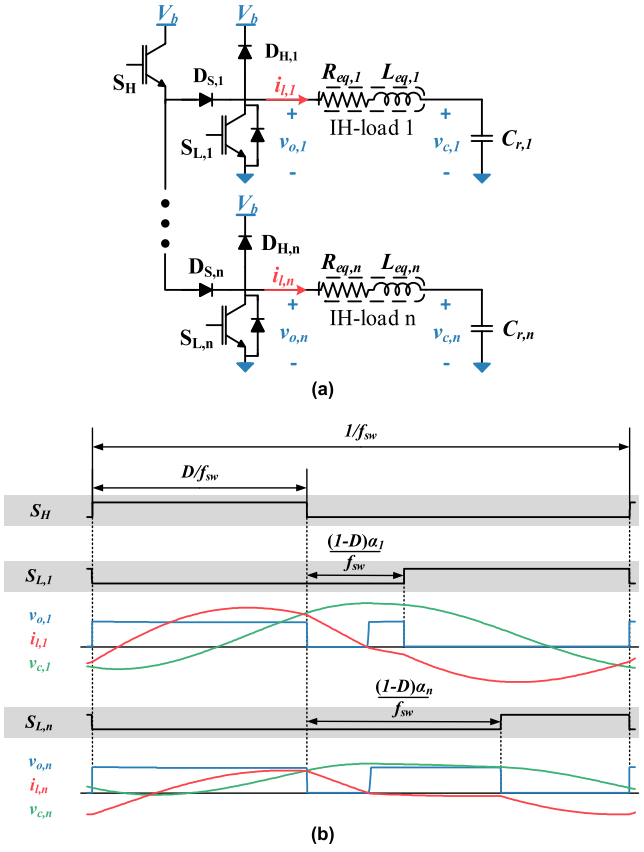

FIGURE 2. Single-column multi-output ZVS matrix resonant converter (a), and the proposed modulation parameters and waveforms (b).

A. MATRIX CONVERTER WITH NC-PDC MODULATION

The inverter considered in this paper is derived from the matrix zero-voltage-switching (ZVS) inverter presented in [31]. Its structure is depicted in II (a), and presents a common high-side transistor, S_H, and an independent output cell for each resonant tank. These cells are composed by a low-side transistor, $S_{L,i}$, with antiparallel diode, $D_{L,i}$, a high-side antiparallel diode, $D_{H,i}$, and a series diode, $D_{S,i}$. Each resonant tank comprises the IH-load equivalent resistance, $R_{eq,i}$, and inductance, $L_{eq,i}$, and a resonant capacitor, $C_{r,i}$.

The operation of the inverter ensures that the same voltage is applied to all resonant tanks during S_H active time while, once S_H is turned off, the series diode allows independent behavior of the different IH loads. The presence of the series diode sets $S_{L,i}$ as the only path to discharge $C_{r,i}$ below the bus voltage, V_{cc}, allowing to control the transmitted power or even disconnect the IH load by modulating $S_{L,i}$ active time.

Based on that operation principle, several modulation strategies have been proposed on the literature [32]. In this paper, non-complementary pulse delay control (NC-PDC) modulation is selected. On it, switching frequency, f_{sw}, and duty cycle, D, are set common to all branches by means of the activation of the high-side transistor, and α_i parameter, which corresponds with $S_{L,i}$ activation delay, allows to achieve independent power control for the different loads (Figure 2(b)).

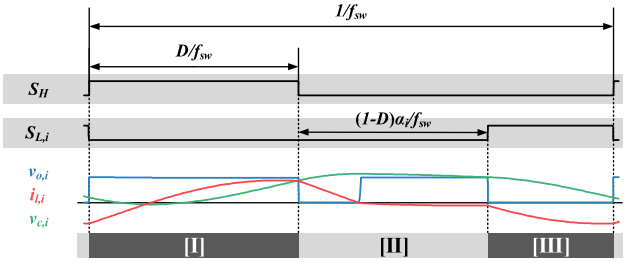

FIGURE 3. Optimization interval division of a switching cycle.

III. MPC FOR RESONANT MULTI-OUTPUT INVERTER

Model predictive control is of great applicability on resonant inverters as it can deal with nonlinear systems and includes constraints both on inputs and states. Besides, MPC offers high performance when dealing with a high number of states and inputs.

Standard MPC implementations calculate a series of optimal control inputs $(u_0, \ldots, u_{N-1})$ of the system within a prediction horizon, N, based on the solving of an optimization problem that minimizes a certain cost function, J. This problem, which is solved at each control instance when new states data is available, can be formulated as

$$\begin{aligned} \underset{u_k}{\text{minimize}} \quad & \sum_{k=0}^{N-1} J\left(x_k, u_k\right) \\ \text{subject to} \quad & x_{k+1} = f\left(x_k, u_k\right), \; x_0 = \hat{x}, \\ & g\left(x_k, u_k\right) \leq 0, \\ & \text{for } k = 0, \ldots, N-1. \end{aligned} \tag{1}$$

where x_k and u_k are the states and the control inputs of the system at step k, respectively. Function $f(x_k,u_k)$ denotes a discrete-time model of the system and g are general constraints to be satisfied during operation. The current state of the system is $\hat{x}$, which needs to be measured or estimated.

A. MODEL OF SINGLE OUTPUT

Each branch presents its own resonant tank. Thus, the dynamics of the i^{th} IH load can be expressed by means of the differential equations of two states, $i_{l,i}$ and $v_{c,i}$:

$$\begin{aligned} \frac{di_{l,i}}{dt} &= \frac{1}{L_{eq,i}}\left(v_{o,i} - R_{eq,i} i_{o,i} - v_{c,i}\right), \\ \frac{dv_{c,i}}{dt} &= \frac{1}{C_r} i_{o,i}, \end{aligned} \tag{2}$$

being the voltage applied to the load, $v_{o,i}$, a signal that changes between 0 V and V_{cc} during the switching period depending on the control parameters, resulting on a switching system. In the case of the proposed converter, f_{sw} and D appear as common control parameters for all branches, as they share high-side transistor activation, and α_i is the control parameter that ensures independent power control.

In [23] a double time transformation is proposed to overcome the challenge of efficiently solving an optimization problem that includes such switching systems when $v_{o,i}$ is known in advance. However, as a consequence of using a non-complementary modulation, while no transistor is active, $v_{o,i}$, depends on the current path as follows:

$$v_{o,i} = \begin{cases} V_{cc} & \text{if } i_{l,i} \leq 0 \\ 0 & \text{if } i_{l,i} > 0. \end{cases} \tag{3}$$

Therefore, a time transformation is performed to divide each switching cycle into three optimization intervals, which are depicted in Figure 3:

$$\begin{aligned} x_{k+1}^{[\mathrm{I}]} &= \frac{D_k}{f_{sw,k}} f^{[\mathrm{I}]}\left(x_k, u_k\right), \\ x_{k+1}^{[\mathrm{II}]} &= \frac{\left(1-D_k\right)\alpha_{i,k}}{f_{sw,k}} f^{[\mathrm{II}]}\left(x_k, u_k\right), \\ x_{k+1}^{[\mathrm{III}]} &= \frac{\left(1-D_k\right)\left(1-\alpha_{i,k}\right)}{f_{sw,k}} f^{[\mathrm{III}]}\left(x_k, u_k\right), \end{aligned} \tag{4}$$

where $f^{[\mathrm{I}]}$ and $f^{[\mathrm{III}]}$ refer to the model defined in (2) with the signal $v_{o,i}$ set to V_{cc} and 0 V respectively. $f^{[\mathrm{II}]}$ also denotes the model defined in (2) but in this case, the signal $v_{o,i}$ is defined by its dependence on the current.

This voltage change has been modelled in the literature by a sigmoid function in order to achieve continuity [33]. $v_{o,i}$ in $f^{[\mathrm{II}]}$ is approximated by a logistic function with a certain slope, λ, which is adjusted by the time transformation:

$$v_{o,i} = \frac{1}{1 + e^{-\lambda\left(\left(1-D_k\right)\alpha_{i,k}/f_{sw,k}\right) i_{l,i}}}. \tag{5}$$

The sigmoid slope is critical for the efficient solving of the optimization problem as steep approximations present big changes for small optimizer steps. In Figure 4 the main waveforms of the converter, obtained using the differential equations of the three intervals and different slopes, are compared with a spice simulation, which shows a good agreement with the real behavior. Due to its direct dependency with $v_{o,i}$, the

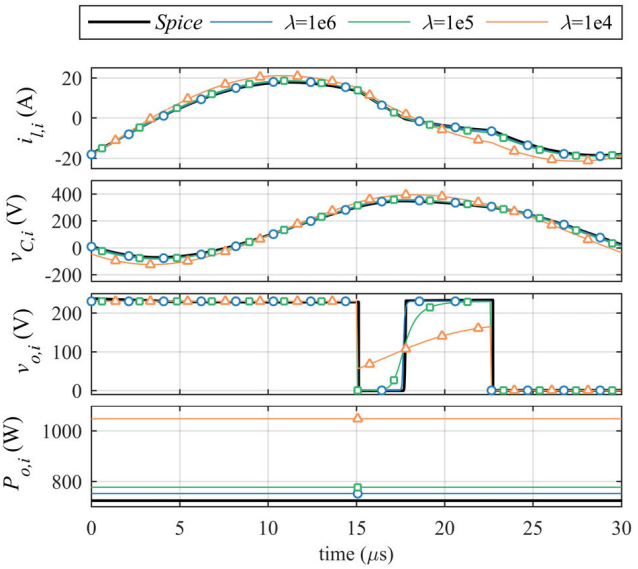

FIGURE 4. Sigmoid steepness and state behavior.

TABLE 1. Sigmoid approximation error comparison.

Model slope, λ	Optimizer runtime (ms)	Simulator error at sampling point		
		$i_{l,i}$ (A)	$v_{c,i}$ (V)	$P_{o,i}$ (W)
1e6	750	0.26	3.83	25.32
1e5	656	0.73	11.21	44.03
1e4	629	2.10	30.31	126.71

transmitted power present a high increase of the error when reducing the slope. However, when using the proposed models on an optimization problem, fastest results are obtained for lower slopes, as presented on Table 1 resulting on a tradeoff that must be considered when selecting the desired slope.

The complete MPC model formulation can be obtained by concatenating the optimizer intervals and assuming that the control parameters are constant during a switching cycle:

$$x_{k+1}^{[mpc]} = \begin{cases} \frac{D_k}{f_{sw,k}} f^{[\mathrm{I}]}\left(x_k, u_k\right) & \text{if mod } (k,3) = 0 \\ \frac{(1-D_k)\alpha_{i,k}}{f_{sw,k}} f^{[\mathrm{II}]}\left(x_k, u_k\right) & \text{if mod } (k,3) = 1 \\ \frac{(1-D_k)(1-\alpha_{i,k})}{f_{sw,k}} f^{[\mathrm{III}]}\left(x_k, u_k\right) & \text{if mod } (k,3) = 2 \end{cases} \tag{6}$$

To incorporate the continuous time ordinary differential equations (6) in our discrete MPC formulation (1), a discretization with orthogonal collocation on finite elements has been performed [34].

As a consequence of this discretization, the average transmitted power, $P_{o,i}$, which is the controller tracking parameter, requires a two-step calculation. The average power at each control interval is obtained by using the value of the states at the collocation points, c:

$$P_{o,i,k} = \sum_{c=1}^{n_{col}} v_{o,i,k}^{[c]} i_{l,i,k}^{[c]} \left(\tau_k^{[c]} - \tau_k^{[c-1]}\right), \tag{7}$$

where n_{col} denotes the number of collocation points and the integral is approximated by a numerical integration in which $\tau_k^{[c]}$ denotes the time of collocation point c in the control interval k. And the average power for the switching cycle is calculated by applying the previously described time transformation to each of the non-zero $v_{o,i}$ control intervals:

$$P_{o,i} = P_{o,i,k|\ \mathrm{mod}\ (k,3)=0}\, D_k + P_{o,i,k|\ \mathrm{mod}\ (k,3)=1}\ (1-D_k)\, \alpha_{i,k}. \tag{8}$$

B. MPC OF THE MULTI-OUTPUT INVERTER

The complete MPC problem is intended to represent a multi-output inverter with any number of branches and to achieve proper efficiency-oriented power tracking.

The optimization problem to solve at the beginning of each switching cycle can be presented as follows:

$$\begin{aligned} \underset{f_{sw,k}, D_k, \alpha_{i,k}}{\text{minimize}} \sum_{k=0}^{N} \sum_{i=0}^{n_{branch}} \Bigg(& \left(P_{o,i,k} - P_{o,i}^{des}\right)^2 + C_1 \alpha_{i,k} \\ & + C_2 f_{sw,k} \left(i_{l,i,k|\ \mathrm{mod}\ (k,3)=1} - i_{l,i,k|\ \mathrm{mod}\ (k,3)=0}\right)\Bigg) \end{aligned}$$

$$\begin{aligned} \text{subject to} \quad & \text{model in (5)} \\ & 30 \le f_{sw,k} \le 70\text{kHz}, \\ & 0.1 \le D_k \le 0.9, \\ & 0.05 \le \alpha_{i,k} \le 0.9, \\ & f_{sw,k} = f_{sw,k-1}, \text{ if mod}(k,3) = 1, 2, \\ & D_k = D_{k-1}, \text{ if mod}(k,3) = 1, 2, \\ & \alpha_{i,k} = \alpha_{i,k-1}, \text{ if mod}(k,3) = 1, 2, \\ & i_{l,i,k} \ge 0, \text{ if mod}(k,3) = 1, \\ & i_{l,i,k} \le 0, \text{ if mod}(k,3) = 0. \end{aligned} \tag{9}$$

On (9), the cost function includes three terms with weighting parameters, C_1 and C_2, to set the relative relevance of each of them. The power tracking term is squared as it penalizes negative and positive deviations equally. The second term is related to the cohexistence of low side transistor ZVS and α_i as control parameter, and aims to minimize the number of hard-switching turn on transitions. Last, the product of f_{sw} and $i_{l,i,k|\mathrm{mod}(k,3)=1}$ and $-i_{l,i,k|\mathrm{mod}(k,3)=2}$ represent a figure of merit (FOM) for the power loses due to the transisor turn off. This FOM is always positive as it is constrained by the ZVS imposition.

The constraints included in (9) can be divided in different groups. The input constraints to limit the optimizer solution to feasible ones, the input constraints to ensure thet the inputs are kept constant within each switching cycle, and constraints to achieve an overall high efficiency solution.

The efficiency constraints are related to ZVS transistor activation. This soft-switching commutation eliminates transistor turn-on losses by ensuring that the associated antiparallel diode is conducting during the turn-on sequence, and therefore, there is no voltage drop in the transistor. Therefore, it is achieved by ensuring the correct current sign at the beginning of control interval. This is especially relevant for $\mathrm{S_H}$ as it is a shared activation component with higher current levels, thus ZVS is achieved by setting $i_{l,i,k} \le 0$ if mod$(k,3) = 0$. For the case of $\mathrm{S_{L,i}}$, NC-PDM modulation strategy requires $\mathrm{D_{H,i}}$ conduction. Therefore, $\mathrm{D_{S,i}}$, is not necessarily conducting and ZVS cannot be ensured for all cases. However, the number of hard-switching commutation can be minimized by implementing it as a soft constraint. In order to do so, $i_{l,i,k} \ge 0$ if mod$(k,3) = 1$ and the α_i term is added to the cost function.

C. MPC TUNING, SIMULATION AND VALIDATION

In this paper, the optimization problems are solved by using an interior point algorithm which is implemented in IPOPT. All the derivative information is computed using automatic differentiation via CasADi [35] and the MPC is implemented using the toolbox do-mpc [36].

Additionally, as the MPC controller is conceived for a DNN implementation, a constraint that ensures that $\mathrm{S_H}$ on time is enough to evaluate the DNN can be added in the form of $f_{sw,k} D_k \ge t_{NN}$.

The prediction horizon is set to five switching intervals, i.e. $N = 15$, as it is considered enough for the system to reach the

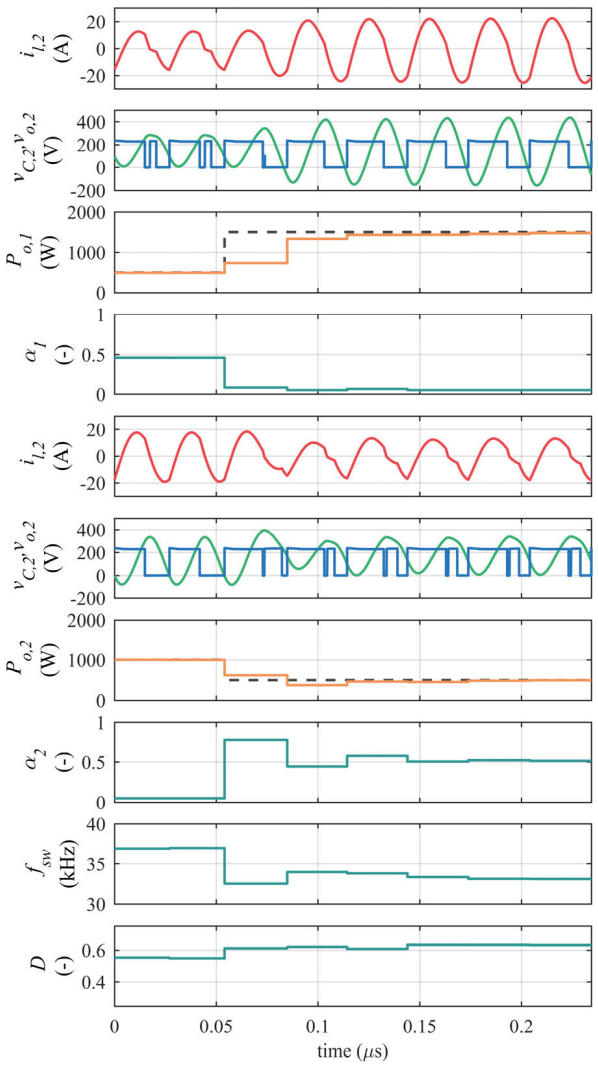

FIGURE 5. Performance of the propossed MPC+P controller during a setpoint change, from $P_{o,1}^{des} = 500$ W $P_{o,2}^{des} = 1000$ W to $P_{o,1}^{des} = 1500$ W $P_{o,2}^{des} = 500$ W.

steady state. The tuning parameters are chosen as $C_1 = 1 \cdot 10^4$ and $C_2 = 1 \cdot 10^{-3}$ in order to balance the relative contributions in the cost function.

The parameters for the MPC model consider equal pot material in all branches. Thus, $V_{cc} = 230$ V, $L_{eq,i} = 68.5\ \mu$H, $R_{eq,i} = 4.6\ \Omega$, and $C_r = 400$ nF.

Additionally, the sigmoid slope is $\lambda = 1e5$ to achieve faster resolution, which is required for the DNN data generation. In order to minimize the approximation error, an additional proportional controller, with a proportionality constant, K, can be implemented, which varies the setpoint given to the MPC, $P_{o,i}^{MPC}$, based on the difference between the desired power, $P_{o,i}^{des}$, and the measured one, $P_{o,i}^{meas}$.

$$P_{o,i}^{MPC} = P_{o,i}^{MPC} + K\left(P_{o,i}^{des} - P_{o,i}^{meas}\right) \tag{10}$$

The controller simulation is performed considering a two-branch inverter. In order to increase the simulation precision a spice model is used. Therefore, LTspice is launched every switching cycle with the calculated control parameters and the previous value of the state variables and provides the new values of the state variables and an accurate power calculation.

TABLE 2. Load uncertanity error.

Load equivalent parameters	Average tracking error (%)		Average SH ZVS (%)	Average SL ZVS (%)
Base simulation	7.84	8.19	100	93.56
$1.15L_{eq,1}$	32.28	8.40	100	95.47
$1.15R_{eq,1}$	14.11	9.06	100	92.59
$0.85L_{eq,1}$	7.91	11.07	100	64.24
$0.85R_{eq,1}$	3.50	8.13	100	91.09
With P controller (10)	0.73	0.76	100	92.05
$1.15L_{eq,1}$	9.99	1.66	100	91.50
$1.15R_{eq,1}$	1.46	0.85	100	90.54
$0.85L_{eq,1}$	1.69	1.17	100	67.26
$0.85R_{eq,1}$	0.75	1.00	100	89.45

The load equivalent parameters for the spice model are $L_{eq,i} = 68.5\ \mu$H, and $R_{eq,i} = 2\pi f_{sw} L_{eq,i}/Q_i$ with Q_i =3.27, which is a more accurate approximation of the IH load behavior.

The simulation of a setpoint change is shown in Figure 5. There can be seen a proper power tracking that respects the SH ZVS constraints and presents at least one branch with SL,i ZVS behavior during the steady state. In Table 2 the results for a longer simulation with more setpoint variations are shown. This table also includes a robustness analysis to show the controller proper behavior with low accuracy in an IH load equivalent parameter estimation.

IV. NEURAL NETWORK IMPLEMENTATION

As aforementioned, to achieve an efficient implementation, the approximation of the high-performance MPC using DNNs is proposed. The selected neural network operates with the current state of the system, i.e. the measured state variables $v_{c,i}$ and $i_{l,i}$, and the desired power, $P_{o,i}^{des}$ as inputs and provides the optimal control inputs for the current switching cycle, f_{sw}, D, and α_i as outputs. Thus, the neural network computation has to be done during S_H active time.

The chosen DNN presents $L = 4$ hidden layers, $M = 30$ neurons per layer and *tanh* is selected as the activation function.

A. DATA GENERATION AND TRAINING

As the intended behavior of the DNN is to approximate the control law, the data pairs for training are generated by the simulation of closed loop operation with various setpoint changes between random $P_{o,i}^{des}$ within the interval [0 2000] W. Therefore, the state variables are dependent of the previous setpoint and MPC solution. The generated training inputs can be seen in Figure 7 where the different power setpoints are represented for the different states, $i_{l,i}$ and $v_{c,i}$, showing a complete coverage of the operation region and an a non-homogeneous distribution that improves stead-state stability.

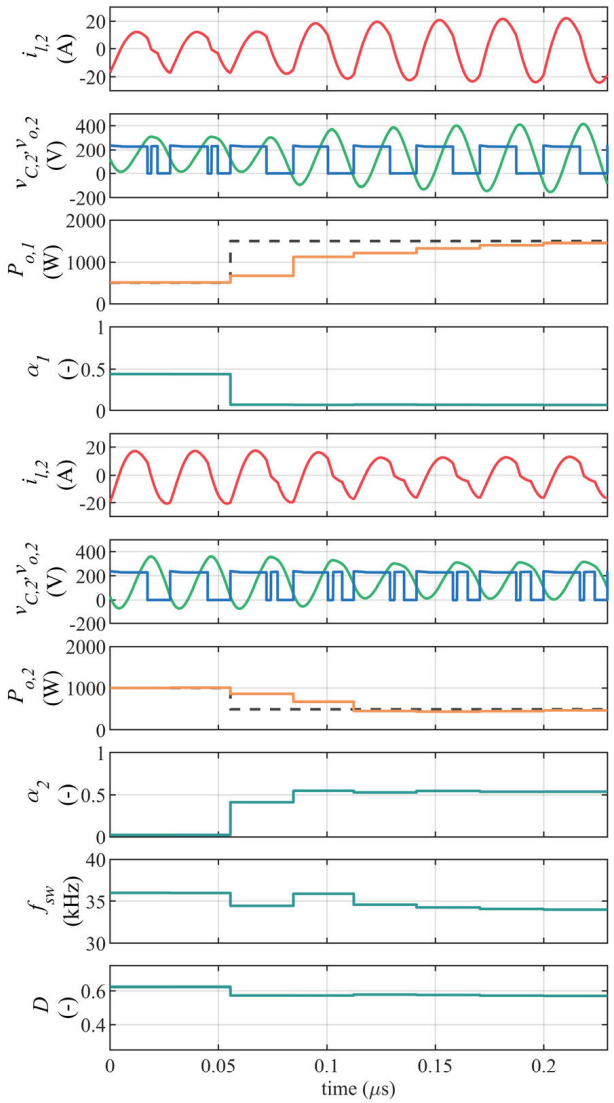

FIGURE 6. Performance of the DNN implementation of the MPC controller during a setpoint change, from $P_{o,1}^{des} = 500$ W $P_{o,2}^{des} = 1000$ W to $P_{o,1}^{des} = 1500$ W $P_{o,2}^{des} = 500$ W.

The model used for the simulation matches the MPC one but with a steeper sigmoid slope and Q_i based $R_{eq,i}$ calculation. Additionally, as load simulation parameters are known during training data generation, instead of being cost-function dependent, $S_{L,i}$ ZVS is added as a constraint for the more power-demanding of the branches, improving performance. Finally, a filtering of the training pairs is performed to avoid learning steady state oscillating scenarios.

Two strategies for the training data have been evaluated. Firstly, the direct learning of the control parameters as they have been simulated, i.e. f_{sw}, D, and α_i, and, secondly, the use of a PWM modulator parameters, implemented as a counter and comparator, i.e. converting the control parameters into comparator instants as: D/f_{sw}, $(D+(1-D)\alpha_i)/f_{sw}$, and $1/f_{sw}$.

The training of the neural network is performed using Keras in Tensorflow [37]. In Table 3 the results for the

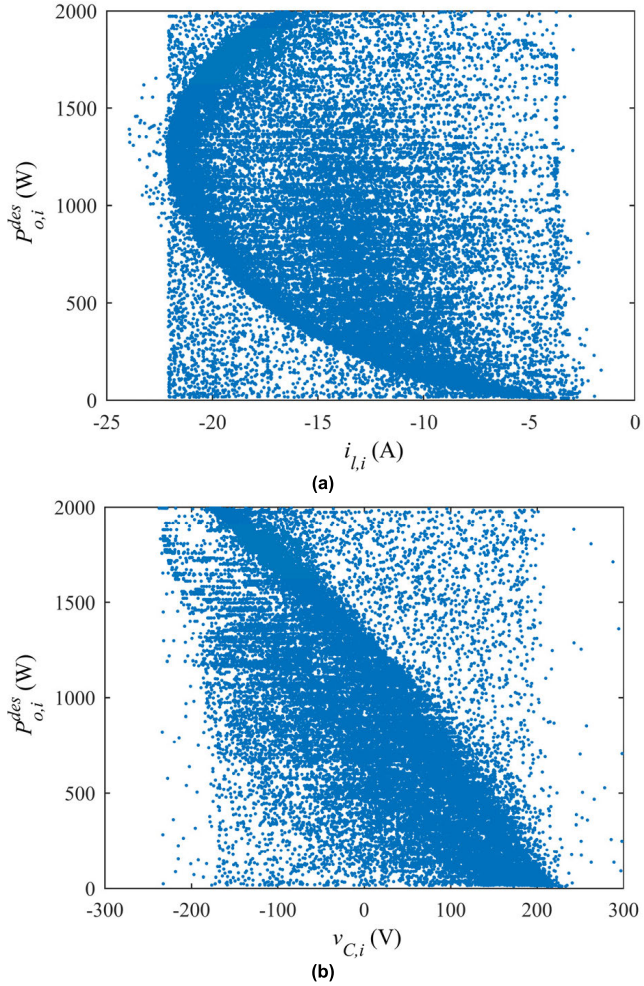

FIGURE 7. Operation region sweep for DNN training data generation. Power setpoint vs the different states, $i_{l,i}$ (a) and $v_{c,i}$ (b).

TABLE 3. Training pairs shape influence.

Data postprocessing	Average test error			
	f_{sw} (kHz)	D (-)	α_1 (-)	α_2 (-)
Sim. format.	0.4361	0.0063	0.0143	0.0160
Comp. format	0.3092	0.0055	0.0152	0.0165

TABLE 4. Training pairs generation performance.

Load equivalent parameters	Average tracking error (%)		Average SH ZVS (%)	Average SL ZVS (%)
Ideal setpoint	10.66	9.52	100	99.72
Real setpoint	1.82	1.73	100	99.45

training with the different control parameter approach can be seen. There, comparator based DNN achieves better results for f_{sw} and the learning differences between the remaining parameters are not significant.

B. DNN SIMULATION AND VALIDATION

The simulation testbench corresponds with the used for the standard MPC controller. In Table 4 the performance results for two training data sets can be seen. The first one consid-

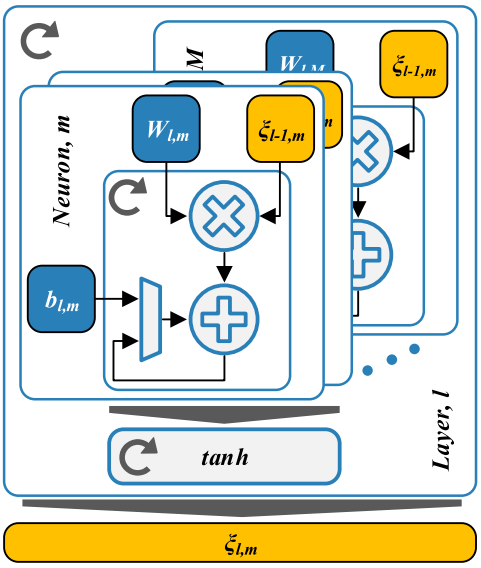

FIGURE 8. DNN main operation blocks.

TABLE 5. DNN implementation resources.

DSP	116	87%
LUTs	32,830	69%
FFs	11,729	12%

ers zero power error in reaching $P_{o,i}^{des}$ when generating the training data and the second one assumes real steady state $P_{o,i}$ as the setpoint. As it can be seen, both cases maintain S_H ZVS and achieve good $S_{L,i}$ ZVS performance, but, additionally, the second approach is able to correct the error due to the model simplification. On III-B the same setpoint change as in the MPC case has been represented to show the proper operation with the real setpoint approximation, i.e. the one that uses $P_{o,i}$.

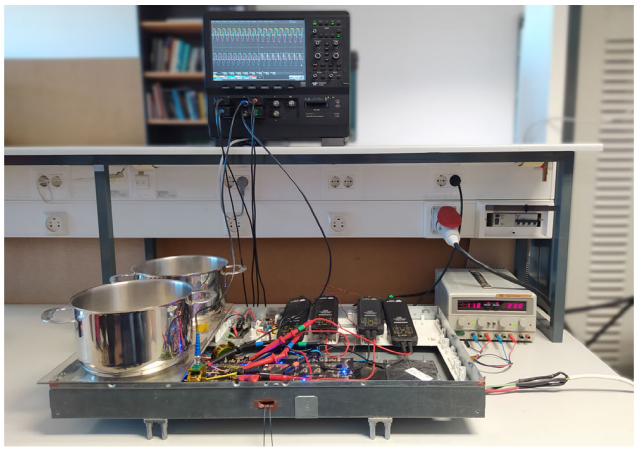

FIGURE 9. Experimental setup.

V. FPGA IMPLEMENTATION AND EXPERIMENTAL RESULTS

When implementing the DNN to control a functioning prototype, a trade-off between computation speed and resource utilization in order to allow a good place and route of the HDL synthesizer is intended. In this paper, the selected FPGA is the Spartan 6 XC6SL75 and the programing file is generated via Xilinx ISE.

A. FPGA IMPLEMENTATION

To achieve a proper behavior, the DNN implementation has to take into account the new input data sensing and output data compatibility with the modulator.

New data sensing is synchronized with S_L deactivation, therefore, ADC time has to be included in the DNN solving time. The normalization of the ADC measurement to the DNN input include the dependences with the sensor offset,

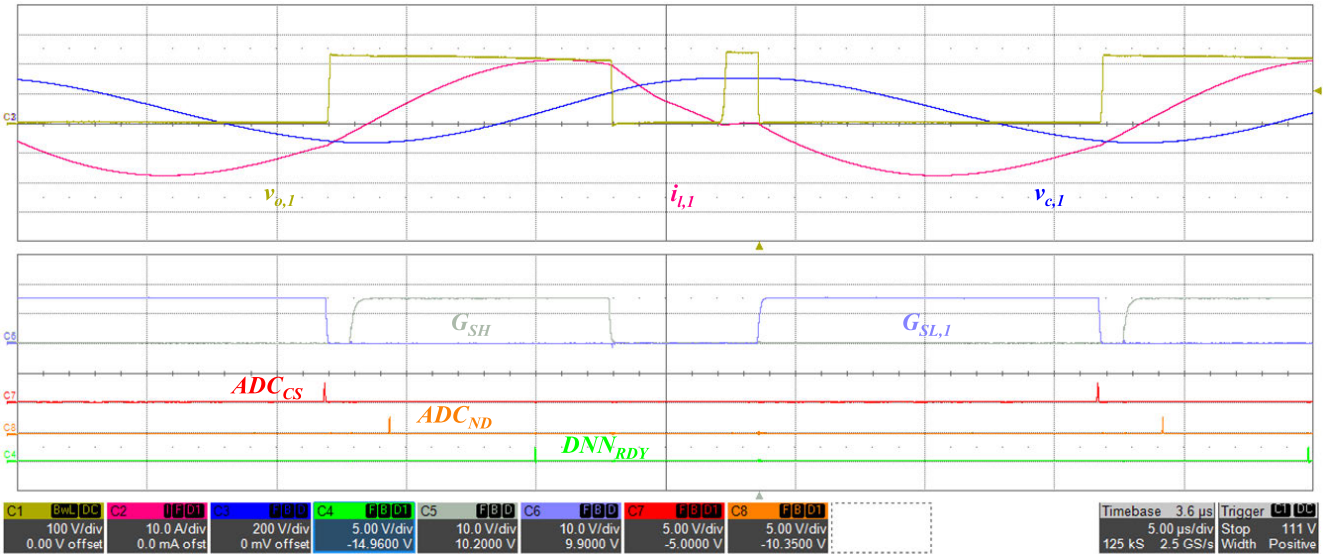

FIGURE 10. Ready signal of the different implementation blocks. From top to bottom: IH load 1 $v_{o,1}$ (100 V/div, yellow), $i_{l,1}$ (10 A/div, pink), and $v_{c,1}$ (200 V/div, dark blue), S_H gate signal, G_{SH} (10 V/div, grey), $S_{L,1}$ gate signal, $G_{SL,1}$ (10 V/div, light blue), ADC capture signal, ADC_{CS} (5 V/div, red), ADC new data signal, ADC_{ND} (5 V/div, orange), and DNN new result signal, DNN_{RDY} (5 V/div, green). Time axis: 5 µs/div.

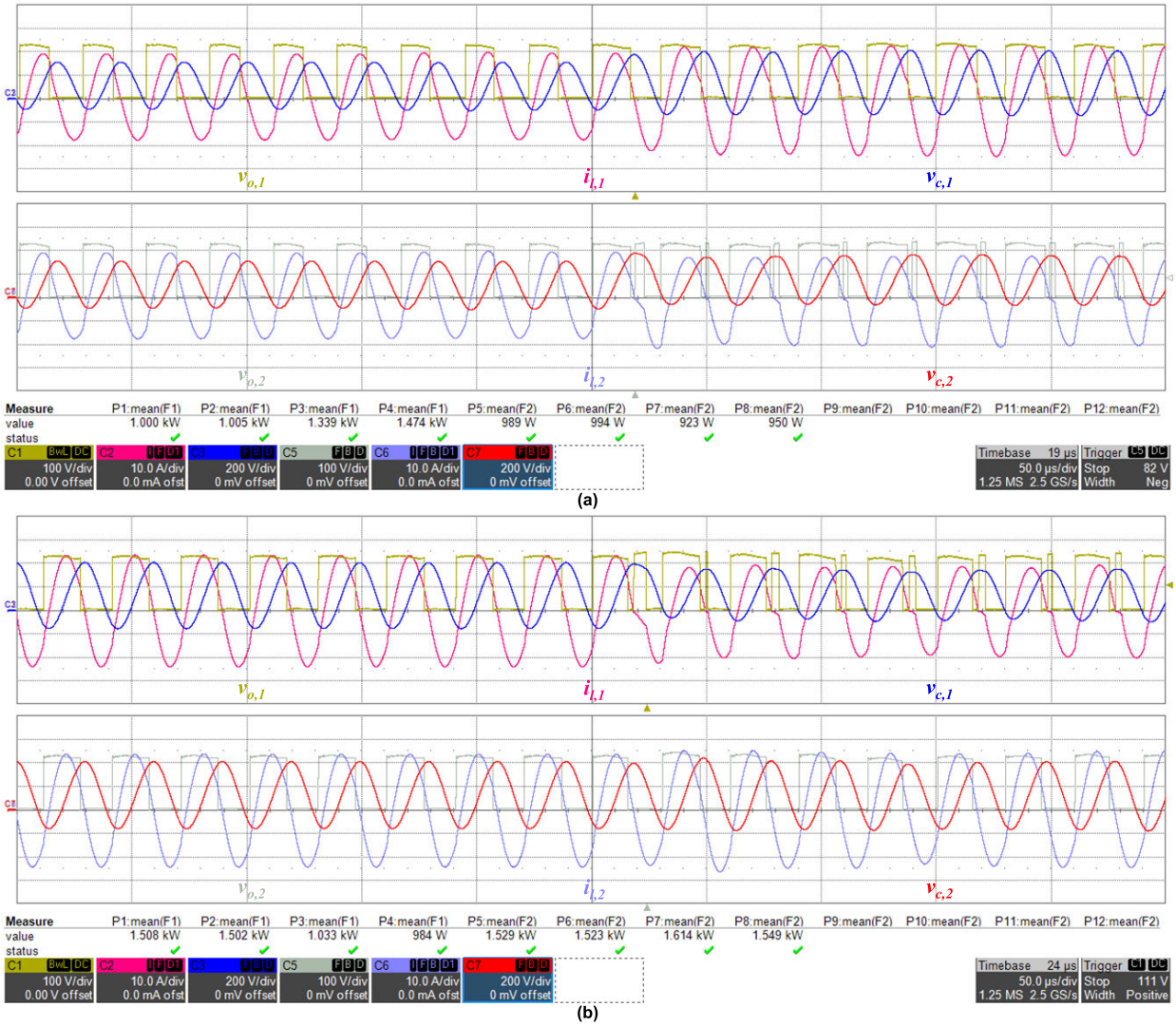

FIGURE 11. Setpoint change to a higher (a) and lower (b) desired power. On each oscilloscope capture, from top to bottom: IH load 1 $v_{o,1}$ (100 V/div, yellow), $i_{l,1}$ (10 A/div, pink), and $v_{c,1}$ (200 V/div, dark blue), and IH load 2 $v_{o,1}$ (100 V/div, grey), $i_{l,1}$ (10 A/div, light blue), and $v_{c,1}$ (200 V/div, red). Time axis: 50 μs/div. Measures P1 to P4 represent the temporal evolution of the transmitted power to IH load 1, $P_{o,1}$, and P5 to P8 represent the temporal evolution of the transmitted power to IH load 2, $P_{o,2}$.

s_{off}, and gain, s_{gain}, leading to a single two step operation

$$\hat{x}_{nn} = \frac{\hat{x}_{ADC}}{s_{gain} range[\hat{x}]} - \left(\frac{s_{offset}}{s_{gain} range[\hat{x}]} + \frac{lower\_bound[\hat{x}]}{range[\hat{x}]} \right) \tag{11}$$

The selected modulator is based on a counter and comparator. Thus, the DNN output only requires to revert the normalization.

The DNN structures is based in the schematic depicted in Figure 8. The operations are implemented as *float32* cores. Each neuron operation is done sequentially in order to limit the carry path length, allowing the multiplier and adder reutilization. Therefore, neuron parallelization is possible with up to 28 neurons, as enough DSP slices are available. Activation function *tanh* is implemented by means of a look up table and is called sequentially by the neurons. The layer calculation time is $n_{in}+ M$ clock cycles. The layers are calculated sequentially, allowing hardware reutilization, as the input of each layer is the output of the previous. Table 5 summarizes the complete implementation resources.

B. EXPERIMENTAL RESULTS

The experimental setup shown in Figure 9 uses the prototype presented in [32] with two connected inductors and two equal material pots on top of each of them.

Figure 10 presents the flags related to the different calculation steps. The upper two are the transistor gate signals, the subsequent two are related to the data acquisition, i.e. measure synchronization and available ADC data, and the last one corresponds with the DNN solution end of calculation. As it can be seen, the ADC sample is synchronized with SL turn off and ADC data transmission and DNN evaluation occur, as expected, during SH on time so the results can be applied in the same switching cycle.

Figure 11 shows the main waveforms in a power stepdown change and a power stepup change starting in equal power

transmission. These waveforms show that ZVS is achieved in S_H turn on and in $S_{L,i}$ turn on when possible, i.e. when both load transmitted power is equal and at least for one branch when the desired power is different. Additionally, both captures include the power measurements corresponding to differently spaced switching cycles, where the power setpoint change can be appreciated. When compared with the simulation results, the main differences arise on the transmitted power error increase, which is a consequence of the mismatch between the real induction load and the simulation model. For example, while equivalent parameters $R_{eq,i}$ and $L_{eq,i}$ are considered constant for simulation, they present a high dependency on the pot temperature. In order to decrease this error, the proportional controller proposed in (10), which presents good results on simulation, can be implemented.

VI. CONCLUSION

The widespread of flexible surface induction heating cooktops is paired with the development of cost-effective versatile multi-output converters. These converters require complex control strategies in order to operate with high efficiency.

In this paper a MPC control strategy for a multi-output ZVS resonant converter operating with a non-complementary modulation has been proposed and analyzed and its implementation with a DNN has been evaluated via simulation and experimental results.

The controller has proven to achieve proper desired power tracking while ensuring ZVS commutation in the shared high side transistor, increasing efficiency by reducing power losses in said critical device. Additionally, ZVS in low side transistor is ensured in steady state for at least one of them. The proposed strategy has been tested using a domestic induction heating prototype operating under real operating conditions, proving the feasibility of the proposed control strategy and implementation.

REFERENCES

[1] H. N. Pham, H. Fujita, K. Ozaki, and N. Uchida, "Dynamic analysis and control for resonant currents in a zone-control induction heating system," *IEEE Trans. Power Electron.*, vol. 28, no. 3, pp. 1297–1307, Mar. 2013.

[2] F. Forest, E. Laboure, F. Costa, and J. Y. Gaspard, "Principle of a multi-load/single converter system for low power induction heating," *IEEE Trans. Power Electron.*, vol. 15, no. 2, pp. 223–230, Mar. 2000.

[3] O. Lucia, J. Acero, C. Carretero, and J. M. Burdio, "Induction heating appliances: Toward more flexible cooking surfaces," *IEEE Ind. Electron. Mag.*, vol. 7, no. 3, pp. 35–47, Sep. 2013.

[4] F. P. Dawson and P. Jain, "A comparison of load commutated inverter systems for induction heating and melting applications," *IEEE Trans. Power Electron.*, vol. 6, no. 3, pp. 430–441, Jul. 1991.

[5] A. K. Lefedjiev and L. Hobson, "Single ended resonant power supply for induction heating," *Electron. Lett.*, vol. 26, no. 12, pp. 814–816, Jun. 1990.

[6] I. Millan, D. Puyal, J. M. Burdio, C. Bemal, and J. Acero, "Improved performance of half-bridge series resonant inverter for induction heating with discontinuous mode control," in *Proc. 22nd Annu. IEEE Appl. Power Electron. Conf. Expo.*, Feb./Mar. 2007, pp. 1293–1298.

[7] S. Zenitani, M. Okamoto, E. Hiraki, and T. Tanaka, "A charge boost type multi output full bride high frequency soft switching inverter for IH cooking appliance," in *Proc. 14th Int. Power Electron. Motion Control Conf.*, Sep. 2010, pp. T2-127–T2-133.

[8] H. Sarnago, O. Lucia, A. Mediano, and J. M. Burdio, "Design and implementation of a high-efficiency multiple-output resonant converter for induction heating applications featuring wide bandgap devices," *IEEE Trans. Power Electron.*, vol. 29, no. 5, pp. 2539–2549, May 2014.

[9] Y.-C. Jung, "Dual half bridge series resonant inverter for induction heating appliance with two loads," *Electron. Lett.*, vol. 35, no. 16, pp. 1345–1346, Aug. 1999.

[10] V. B. Devara, V. Neti, T. Maity, and P. Shunmugam, "Capacitor-sharing two-output series-resonant inverter for induction cooking application," *IET Power Electron.*, vol. 9, no. 11, pp. 2240–2248, Sep. 2016.

[11] F. Forest, S. Faucher, J.-Y. Gaspard, D. Montloup, J.-J. Huselstein, and C. Joubert, "Frequency-synchronized resonant converters for the supply of multiwinding coils in induction cooking appliances," *IEEE Trans. Ind. Electron.*, vol. 54, no. 1, pp. 441–452, Feb. 2007.

[12] S. H. Hosseini, A. Goharrizi, and E. Karimi, "A multi-output series resonant inverter with asymmetrical voltage-cancellation control for induction-heating cooking appliances," in *Proc. 5th Int. Power Electron. Motion Control Conf.*, Aug. 2006, pp. 1–6.

[13] S. K. Papani, V. Neti, and B. K. Murthy, "Dual frequency inverter configuration for multiple-load induction cooking application," *IET Power Electron.*, vol. 8, no. 4, pp. 591–601, Apr. 2015.

[14] J. B. Rawlings, D. Q. Mayne, and M. Diehl, *Model Predictive Control: Theory, Computation, and Design*. Madison, WI, USA: Nob Hill Publishing, LLC, 2017.

[15] S. Kouro, M. A. Perez, J. Rodriguez, A. M. Llor, and H. A. Young, "Model predictive control: MPC's role in the evolution of power electronics," *IEEE Ind. Electron. Mag.*, vol. 9, no. 4, pp. 8–21, Dec. 2015.

[16] Ó. Lucía, E. Monmasson, D. Navarro, L. A. Barragan, I. Urriza, and J. I. Artigas, "Modern control architectures and implementation," in *Control of Power Electronic Converters and Systems*. London, U.K.: Academic Press, 2018.

[17] S. Vazquez, J. Rodriguez, M. Rivera, L. G. Franquelo, and M. Norambuena, "Model predictive control for power converters and drives: Advances and trends," *IEEE Trans. Ind. Electron.*, vol. 64, no. 2, pp. 935–947, Feb. 2017.

[18] S. Vazquez, J. I. Leon, L. G. Franquelo, J. Rodriguez, H. A. Young, A. Marquez, and P. Zanchetta, "Model predictive control: A review of its applications in power electronics," *IEEE Ind. Electron. Mag.*, vol. 8, no. 1, pp. 16–31, Mar. 2014.

[19] B. Karg and S. Lucia, "Efficient representation and approximation of model predictive control laws via deep learning," *IEEE Trans. Cybern.*, vol. 50, no. 9, pp. 3866–3878, Sep. 2020.

[20] S. Chen, K. Saulnier, N. Atanasov, D. D. Lee, V. Kumar, G. J. Pappas, and M. Morari, "Approximating explicit model predictive control using constrained neural networks," in *Proc. Annu. Amer. Control Conf. (ACC)*, Jun. 2018, pp. 1520–1527.

[21] M. Hertneck, J. Kohler, S. Trimpe, and F. Allgower, "Learning an approximate model predictive controller with guarantees," *IEEE Control Syst. Lett.*, vol. 2, no. 3, pp. 543–548, Jul. 2018.

[22] S. Lucia, D. Navarro, Ó. Lucía, P. Zometa, and R. Findeisen, "Optimized FPGA implementation of model predictive control for embedded systems using high-level synthesis tool," *IEEE Trans. Ind. Informat.*, vol. 14, no. 1, pp. 137–145, Jan. 2018.

[23] S. Lucia, D. Navarro, B. Karg, H. Sarnago, and O. Lucia, "Deep learning-based model predictive control for resonant power converters," *IEEE Trans. Ind. Informat.*, vol. 17, no. 1, pp. 409–420, Jan. 2021.

[24] Ó. Lucía, J. M. Burdío, L. A. Barragán, J. Acero, and I. Millán, "Series-resonant multiinverter for multiple induction heaters," *IEEE Trans. Power Electron.*, vol. 25, no. 11, pp. 2860–2868, Nov. 2010.

[25] J. M. Burdío, F. Monterde, J. R. Garcia, L. A. Barragan, and A. Martinez, "A two-output series-resonant inverter for induction-heating cooking appliances," *IEEE Trans. Power Electron.*, vol. 20, no. 4, pp. 815–822, Jul. 2005.

[26] T. Hirokawa, E. Hiraki, T. Tanaka, M. Imai, K. Yasui, and S. Sumiyoshi, "Dual-frequency multiple-output resonant soft-switching inverter for induction heating cooking appliances," in *Proc. 39th Annu. Conf. IEEE Ind. Electron. Soc. (IECON)*, Nov. 2013, pp. 5028–5033.

[27] H. Sarnago, J. M. Burdío, and Ó. Lucía, "High-performance and cost-effective ZCS matrix resonant inverter for total active surface induction heating appliances," *IEEE Trans. Power Electron.*, vol. 34, no. 1, pp. 117–125, Jan. 2019.

[28] Ó. Lucía, C. Carretero, J. M. Burdío, J. Acero, and F. Almazan, "Multiple-output resonant matrix converter for multiple induction heaters," *IEEE Trans. Ind. Appl.*, vol. 48, no. 4, pp. 1387–1396, Jul. 2012.

[29] H. Sarnago, O. Lucia, and J. M. Burdio, "Multiresonant power converter for improved dual-frequency induction heating," *IEEE Trans. Power Electron.*, vol. 34, no. 3, pp. 2097–2103, Mar. 2019.
[30] P. Guillen, H. Sarnago, O. Lucia, and J. M. Burdio, "Mains-synchronized pulse density modulation strategy applied to a ZVS resonant matrix inverter," *IEEE Trans. Ind. Electron.*, vol. 68, no. 11, pp. 10835–10844, Nov. 2021.
[31] H. Sarnago, P. Guillen, J. M. Burdio, and O. Lucia, "Multiple-output ZVS resonant inverter architecture for flexible induction heating appliances," *IEEE Access*, vol. 7, pp. 157046–157056, 2019.
[32] P. Guillen, H. Sarnago, O. Lucia, and J. M. Burdio, "Asymmetrical noncomplementary modulation strategies for independent power control in multioutput resonant inverters," *IEEE J. Emerg. Sel. Topics Power Electron.*, vol. 9, no. 1, pp. 629–637, Feb. 2021.
[33] Y. Lu, X. Huang, Y. Huang, and D. Liu, "Sigmoid function model for a PFM power electronic converter," *IEEE Trans. Power Electron.*, vol. 35, no. 4, pp. 4233–4241, Apr. 2020.
[34] L. T. Biegler, *Nonlinear Programming: Concepts, Algorithms, and Applications to Chemical Processes* (MOS-SIAM Series on Optimization). Philadelphia, PA, USA: SIAM, 2010.
[35] J. Andersson, J. Åkesson, and M. Diehl, "CasADi: A symbolic package for automatic differentiation and optimal control," in *Recent Advances in Algorithmic Differentiation*. Berlin, Germany: Springer, 2012, pp. 297–307.
[36] S. Lucia, A. Tătulea-Codrean, C. Schoppmeyer, and S. Engell, "Rapid development of modular and sustainable nonlinear model predictive control solutions," *Control Eng. Pract.*, vol. 60, pp. 51–62, Mar. 2017.
[37] F. Chollet. *Keras*. Accessed: Nov. 6, 2021. [Online]. Available: https://github.com/fchollet/keras

PABLO GUILLÉN (Student Member, IEEE) received the M.Sc. degree in industrial engineering from the University of Zaragoza, Zaragoza, Spain, in 2017, where he is currently pursuing the Ph.D. degree with the Department of Electronic Engineering and Communications.

Since 2017, he held a research internship with the Bosch and Siemens Home Appliances Group. He was a Visiting Scholar with TU Dortmund, Germany, in 2021. His research interests include resonant power converters and digital control applied to induction heating.

Mr. Guillén is a member of the Aragon Institute for Engineering Research (I3A).

FELIX FIEDLER received the B.Sc. and M.Sc. degrees in energy- and process engineering from Technische Universität Berlin, Germany, in 2015 and 2018, respectively. He is currently pursuing the Ph.D. degree with Technische Universität Dortmund.

After his master's degree, he was admitted into the HEIBRiDs Graduate School Doctoral Program for Data Science, with association to the Einstein Center for Digital Future, Technische Universität Berlin, and the German Aerospace Center (DLR). Since 2020, he has been working as a Research Assistant with Technische Universität Dortmund. In his research, he is leveraging novel methods from machine learning for data-based system identification in advanced control applications.

HÉCTOR SARNAGO (Senior Member, IEEE) received the M.Sc. degree in electrical engineering and the Ph.D. degree in power electronics from the University of Zaragoza, Spain, in 2010 and 2013, respectively.

Currently, he is a Senior Postdoctoral Researcher with the Department of Electronic Engineering and Communications, University of Zaragoza. His research interests include resonant converters and digital control for induction heating applications.

Dr. Sarnago is a member of the Aragon Institute for Engineering Research (I3A).

SERGIO LUCÍA (Member, IEEE) received the M.Sc. degree in electrical engineering from the University of Zaragoza, Spain, in 2010, and the Dr. (Ing.) degree in optimization and automatic control from TU Dortmund University, Germany, in 2014. He joined the Otto-von-Guericke Universität Magdeburg and visited the Massachusetts Institute of Technology as a Postdoctoral Fellow. He was an Assistant Professor at TU Berlin, between 2017 and 2020. Since 2020, he has been a Professor at TU Dortmund University and the Head of the Laboratory of Process Automation Systems. His research interests include decision-making under uncertainty, process control, and the interplay between machine learning and control theory. He is an Associate Editor of the *Journal of Process Control* and *Optimal Control Applications and Methods*.

ÓSCAR LUCÍA (Senior Member, IEEE) received the M.Sc. and Ph.D. degrees (Hons.) in electrical engineering from the University of Zaragoza, Spain, in 2006 and 2010, respectively.

In 2006 and 2007, he held a research internship at the Bosch and Siemens Home Appliances Group. Since 2008, he has been with the Department of Electronic Engineering and Communications, University of Zaragoza, where he is currently an Associate Professor with accreditation for a Full Professor. He was a Visiting Scholar with the Center for Power Electronics Systems (CPES, Virginia Tech, USA), in 2009 and 2012, and TU Berlin, Germany, in 2019. His research interests include resonant power conversion, wide-bandgap devices, and digital control, mainly applied to wireless power transfer, induction heating, electric vehicles, and biomedical applications. In these topics, he has published more than 100 international journal articles and 170 conference papers, and he has filed 50 international patents.

Dr. Lucía is an Active Member of the Power Electronics (PELS) and Industrial Electronics (IES) Societies. He is a member of the Aragon Institute for Engineering Research (I3A). Currently, he is an Associate Editor of the IEEE TRANSACTIONS ON INDUSTRIAL ELECTRONICS, the IEEE TRANSACTIONS ON POWER ELECTRONICS, *IEEE Industrial Electronics Magazine*, and the IEEE OPEN JOURNAL OF THE INDUSTRIAL ELECTRONICS SOCIETY. He has received the 2020 *IEEE Industrial Electronics Magazine* Best Paper Award and the "Agustín de Betancourt y Molina" Award by the Real Academia de Ingeniería.